Available online at www.sciencedirect.com

ScienceDirect

Ceramics International 41 (2015) 5621–5633

CERAMICS INTERNATIONAL

www.elsevier.com/locate/ceramint

Composite ceramic membranes from natural aluminosilicates for microfiltration applications

M.C. Almandoz[a], C.L. Pagliero[b], N.A. Ochoa[c], J. Marchese[c,*]

[a]Area de Química Física, FQByF (UNSL), Argentina
[b]Departamento de Tecnología Química-Facultad de Ingeniería (UNRC-CONICET), Argentina
[c]Instituto de Física Aplicada – INFAP Departamento de Química Universidad Nacional de San Luis-CONICET, Chacabuco 917, 5700 San Luis, Argentina

Received 30 October 2014; received in revised form 16 December 2014; accepted 26 December 2014
Available online 3 January 2015

Abstract

This work concerns to the development and characterisation of support, active layer and tubular composite membranes (CM) from natural aluminosilicates as principal components (clay, bentonite, feldspar, quartz, alumina). The selection of these raw materials was primarily based on their low cost and they are locally produced. In the substrates preparation, the effect of materials compositions, additives, particle sizes, paste rheological properties, and drying-sintering temperatures was investigated. The consolidated ceramic substrates were characterised by SEM, DTA–TG, X-Ray diffraction, Hg intrusion, mechanical resistance, and water flux measurements. Extrusion has been used as the forming process of tubular support. The CM was fabricated depositing a thin active layer by slip-casting method on the support. The CM sintered at 1200 °C showed the best structural characteristics, porosities of 50%, active layer pore size between 0.08 and 0.55 μm. The CM hydraulic permeabilities (10–274 L/h m^2 kPa) were comparable and greater than several inorganic commercial membranes and CM obtained from other researches. The CM microfiltration effectiveness was tested with different substances from food industry, i.e. slaughterhouse wastewater treatment and goat milk pasteurisation. The obtained results, insoluble residue rejections (100%) and high bacterial removal (87–99%), make the ceramic CM suitable for microfiltration processes.

Keywords: A. Sintering; Aluminosilicates; Ceramic membranes; Composite materials; Microfiltration

1. Introduction

Membrane separation processes extend more every day in industrial uses, with new requirements concerning to materials and preparation procedures. The interest in separation by the use of inorganic membranes has rapidly increased during the last two decades. Due to their potential application in a wide range of industrial processes such as water and effluent treatments [1–5], drink clarification [6–8], milk pasteurisation [9–13], biochemical processing [14,15], inorganic membrane technologies have achieved an increasing importance. Ceramic membranes have many known advantages such as high thermal and chemical stability, pressure resistance, long lifetime, and catalytic properties from their intrinsic nature [16,17].

The main process to prepare ceramic membranes includes first the obtaining of a good dispersion of small particles and then, the deposition of such dispersion on a support by a slip casting method. The support provides mechanical strength to a membrane top-layer (or active layer) to withstand the stress induced by the pressure difference applied over the entire membrane and simultaneously has a low resistance to the filtrate flow. Furthermore, the supports require chemical stability, heat shock-stability and high porosity, among others. For example, ceramic filters can be steam cleaned in applications that require sterility. The high hardness of ceramics also gives them better wear resistance. These properties are similar to those put forward for the use of dense ceramics as structural engineering materials. Macroporous ceramics can be fabricated by ceramic compacts partially sintered which are produced by conventional ceramic techniques. In this case the pore structure is controlled by the packing of particles. The pore size is commonly controlled by the particle size and the

*Corresponding author. Tel.: +54 2652 424689; fax: +54 2652 430224.
E-mail address: marchese@unsl.edu.ar (J. Marchese).

http://dx.doi.org/10.1016/j.ceramint.2014.12.144
0272-8842/

densities are limited to those given by the green density. Usually, the suspensions are prepared from a small distribution of particles and they may be used only after a complete stabilisation. Besides, it is necessary some adequate processes such as mixing, aging and removing the bigger diameter particles. Sometimes organic surfactants are added to avoid the flocculation of the suspensions.

Most of the supports are generally manufactured from compounds such as alumina (Al_2O_3) [18–28], cordierite ($2MgO \cdot 2Al_2O_3 \cdot 5SiO_2$) [29–31]) and mullite ($3Al_2O_3 \cdot 2SiO_2$) [32–33]. These materials have relatively elevated prices which significantly contribute to the cost of membrane modules for industrial applications. To reduce the cost of ceramic membrane fabrication, recent research works are focused on the use of cheaper raw materials such as apatite powder [34], natural raw clay [35–37], dolomite, kaolin [38,39] and waste materials such as fly ash [40–42]. Regarding to mesoporous and microporous ceramics, these materials have pore sizes that range from 50 nm to below 1 nm. This interval of pore size is commonly beyond the pore size ranges for which the powder processing routes are suitable. Alternative approaches include the sol–gel process or the preparation of synthetic zeolites and pillared clays.

To obtain the composite ceramic membrane the active layer has to be deposited on the support. This active layer used in liquid permeation consists of a porous layer, usually symmetric, with a pore density of 10^9 pores/cm^2 approximately and a porosity (or void volume fraction) between 30% and 70%. The pore size is included in a range of 50–1000 nm in the case of MF and 2–50 nm for ultrafiltration (UF) membranes [43].

In order to decrease the membrane cost and to make use of regional raw materials, this work aims to prepare composite ceramic membranes using natural ball clay, bentonite, feldspar, quartz, alumina, and chemical additives. The different substrates (support, active layer, and composite membrane) are prepared controlling the particle size, the paste formulation and the thermal treatment. Their structural and functional properties are determined by different techniques. The most important parameters used in the characterisation of these substrates are: surface and internal morphology, chemical transformation during the thermal process, mean pore size, pore size distribution, porosity and water permeability. The performance of the ceramic composite membranes is analysed through microfiltration tests of different substances from the food industry.

Fig. 1 shows a schematic representation of the sequential steps of the support, active layer, and the procedure of composite membrane preparation. The main manufacture steps include: a) paste formulation, b) paste conditioning (milling, sieving and suspension stabilisation), c) casting, d) drying and sintering.

2. Materials and characterisation techniques

2.1. Raw materials

Clay, quartz, and feldspar used in the present work were provided by Piedra Grande (Argentine). The chemical composition determined by Induction Coupled Plasma (ICP) and

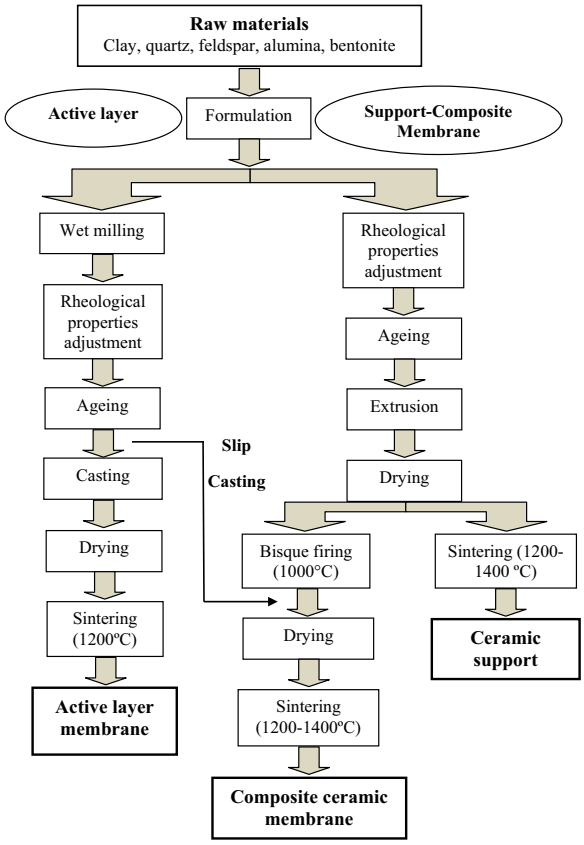

Fig. 1. Schematic representation of support, active layer and composite ceramic membrane preparation.

Atomic Absorption with Graphite Furnace (AA-GF), expressed as weight percentages are [43]; clay: 61% SiO_2, 25% Al_2O_3, 0.7% Fe_2O_3, 1.6% CaO, 0.45% MgO, 0.5% TiO_2, 1.1% K_2O, 0.15% Na_2O and 9.5% of solids lost by calcinations; quartz: SiO_2 was present in a 96–98% (w/w), and low quantities of Al_2O_3 (0.5–1% (w/w)) and alkalis (0.1–0.3% (w/w)); feldspar: 65–70% SiO_2, 16–20% Al_2O_3, 10–14% of alkalis with a Na/K ratio of 3–4, 1–2% oxides of Fe, Mg, Ca and Ti, and 0.2–0.6% component losses by calcinations. Bentonite was supplied by Santa Gema Company (Argentine), and it is composed primarily by silica and aluminium oxide, 0.2–0.5% Fe_2O_3, 1–2% CaO, 1.5–2.5% Na_2O, 3–5% MgO, 1–2% carbonates of Ca and Mg, and humidity of 10–12%. Alumina was provided by Alcoa S.A. (Argentine), and it was obtained from bauxite by the so-called complex process Bayer. It contains more than 98% of Al_2O_3, 0.5–1% Na_2O and 0.05–0.07% ($Fe_2O_3 + SiO_2$). The particle size ranges of these materials obtained by X-Rays analysis are informed in Table 1. The additives magnesium silicate ($MgSiO_4$), sodium silicate (Na_2SiO_4), sodium carbonate (Na_2CO_3), and glycerine were acquired from Aldrich (Argentine).

2.2. Characterisation techniques

To determine the chemical and physical properties of the green pastes and consolidate ceramic substrates, different techniques were used. The substrates were characterised by studying both their structure and functionality.

Table 1
Material particle sizes and paste formulation.

Components	Particle size range (μm)	S1 (%) w/w	S2 (%) w/w	S3 (%) w/w	Active layer (%) w/w
Ball clay	0.2–50	10.0	6.70	6.70	10.0
Bentonite	1–100	5.00	6.70	6.70	2.50
Alumina	50–200	47.0	52.4	52.4	67.5
Quartz	2–300	10.0	9.50	9.50	20.0
Calcium carbonate	30–80	10.0	17.0	17.0	–
Feldspar	1–300	15.0	4.80	4.80	–
Magnesium silicate	–	3.00	2.90	2.90	–
Sodium silicate	–	0.03	0.03	0.03	0.08
Sodium carbonate	–	0.03	0.03	0.03	–
Glycerine	–	8.00	8.00	8.00	–
Average particle diameter, d_p (μm)	–	39.14	22.64	13.38	52.31

2.2.1. Green paste analysis

Particle size distributions of the raw materials and green pastes were measured directly via X-ray absorption with a Micromeritics SediGraph 5100 (USA) apparatus. The application range of measurement, expressed as particle diameter, is from 300 to 0.1 μm. The viscosity of suspensions was measured using a rotary viscometer (DVIII and LVIII, Brookfield Engineering Laboratories Inc., USA) at 298 K. The viscosity applicability range of the instrument is from 15 to 40.000.000 cP.

Differential thermal analysis and thermogravimetric analysis (DTA–TG) of dope samples were made with the Netzsch STA 409PC (Germany) apparatus. Samples with a mass of about 10 mg were used. Heating rate of 10 °C/min was used up to 1000 °C for the measurements.

2.2.2. Substrates structure analysis

Surface, cross section morphology of consolidated substrates (support and active layer) and presence of possible defects were observed by using a scanning electron microscope (JEOL JSM-T300, Japan) at a 750 × magnification. For the cross-section SEM images, samples were fractured and sputter-coated with gold under vacuum (< 0.1 Torr) in an argon atmosphere and 20 mA current, for a period of 2 min.

The porosity and average pore diameter of the sintered substrates were determined using Mercury Intrusion Porosimetry (MIP) with an Autopore III 9410 (Micromeritics Instrument Corporation, USA) porosimeter, working range from 0 to 414 MPa corresponding to a pore sizes from 300 to 0.003 μm.

X-ray diffraction (XRD) technique was used to identify the phase formations after substrate sintering. XRD data were obtained from Siemens D-500X (USA) diffractometer device with Cu K-alpha radiation source and a Secondary beam crystal monochromator. The samples were scanned at diffraction angle 2θ from 1° to 70°. The obtained XRD spectra were matched with the JCPDS data base file.

2.2.3. Mechanical resistance test (MR)

The fracture strength module of the sintered materials was obtained by using a Comten apparatus (USA), model 942KV-C1000. The test was made by the three point bending method according DIN 51030 norms, using parallelepiped sintered pattern bars (0.2 m length and square section of 0.015 m^2) subjected to the same velocity of charge (10 cm/min).

2.2.4. Water flow (WF)

To determine the hydraulic permeability and the hydraulic radius, water flow through tubular substrates was measured. The experimental filtration device at lab-scale has been described elsewhere [44]. The operational conditions were $T=25$ °C and feed rate of 1.5 L/min. The tubular substrate was placed in an appropriated module made of acrylic material. Water was pumped through the inner side of the tubular ceramic substrate using a peristaltic pump. The water flows were determined at different trans-membrane pressures (Δp), an analytical balance interfaced with a computer was used to process permeate mass data vs. time. Assuming cylindrical and parallel pores, the hydraulic permeability (L_h) of the membrane can be estimated with the Hagen–Poiseuille equation as follows:

$$J = \frac{n\pi\, r_h^4 \Delta p}{8\mu l} \tag{1}$$

$$L_h = \frac{Jl}{A\Delta p} = \frac{\varepsilon r_h^2}{8\mu} \tag{2}$$

where J (L m^{-2} s^{-1}) is the water flow density through the membrane, r_h the average hydraulic pore radius, μ is the water viscosity at 25 °C, l is the pore length or membrane thickness, n the pore surface density (number of pores/membrane area), ε ($=n\pi r_h^2$) the porosity of the membrane. When the pore length or membrane thickness is not well defined, the membrane permeability or permeance (L'_h) can be expressed as:

$$L_h^{'} = \frac{J}{A\ \Delta p} = \frac{\varepsilon r_h^2}{8l\mu} \tag{3}$$

The average hydraulic pore radius is evaluated from

$$r_h = \left[\frac{8\mu}{\varepsilon} L_h\right]^{0.5} = \left[\frac{8\mu l}{\varepsilon} L_h^{'}\right]^{0.5} \tag{4}$$

3. Support preparation and characterisation

3.1. Paste formulation

The diverse chemical and physical characteristics of selected raw materials give to the green dope different features, for instance: the presence of fine particles with plaque morphology and organic material in clay and bentonite confers plasticity to the paste. Besides, the high content of alkalis reduces the paste melting point. In contrast, quartz and feldspars provide low plasticity and high refractory properties to the paste. These components reduce the drying time and paste contraction, thus, modifying the aging temperature interval and the substrate properties after sintering. The silica and alumina present in the raw materials form the skeletal structure of the substrates after calcinations. The additive components are electrolytes which in low proportions perform as particle

binding and deflocculants, giving appropriated rheological characteristics to the green dope.

The sintered support must have good mechanical resistance and a high porous structure (porosity higher than 40%). Based on the properties of the raw materials proposed in this research, pastes with different formulations and particle sizes were prepared. After sintering process, only three ceramic paste formulations identified as S1, S2 and S3, have achieved the appropriate structural and mechanical characteristics to be used as ceramic support. These paste compositions expressed in w/w percentage (% without consider the additives) and their particle size range are shown in Table 1.

Lower average particle size for the slurry S3 was obtained by sieving the powders quartz, feldspar and alumina through a Tyler mesh.

The compositions of the S2 and S3 pastes were identical; however they differ in the distribution of particle size and average particle diameter (d_p), 22.64 μm and 13.38 μm for S2 and S3 respectively. The lowest average particle size of the S3 paste was achieved by sieving the powders of quartz, feldspar and alumina through a mesh 140 ASTM E 11-87. S1 and S2 pastes vary on their compositions and on the average particle size ($d_p(S1) > d_p(S2)$). As it was pointed out, clay and bentonite provide plasticity to the membrane; feldspar, quartz and alumina contribute to the mechanical and thermal stability of the substrate. The presence of calcium carbonate allows regulating the porous texture and contributing to a higher porous structure, by dissociation into CaO and CO_2 during the sintered step. On the other hand, sodium carbonate acting as a colloidal agent improves dispersion properties of the inorganic precursors. As a result, more homogeneity in the final substrate structure is acquired. The glycerine is a lubricant agent which allows diminishing the frictional forces between the green dope and the steel material of the extruder during the support casting.

Green dopes were prepared by dispersing and mixing the raw materials in distilled water (10 kg) with a 1:1 solid/water weight ratio, under a constant stirring at 80–90 rpm using a vane mechanical stirrer (Glas-Col®, USA). The raw materials (clay, bentonite, calcium carbonate, feldspar, quartz, and alumina) and the proper amounts of additives in the percentages specified in Table 1 were slowly and sequentially incorporated into the water. The obtained pastes were aged during 48 h at a stirring rate of 200 rpm.

The particle size distributions of the green pastes were measured by X-rays absorption. As expected, a broad and multimodal distribution of particle diameter ranged from 0.1 to 300 μm for the three support pastes was observed. The widespread distributions are mainly attributed to the different particle sizes of the raw materials used in the paste formulation (Table 1).

The thermograms curves from DTA–TG analysis indicated similar behaviour for the three pastes. DTA–TG curves showed a low mass loss when the pastes were heated from 25 to 900 °C. However, three endothermic peaks in DTA curve were also observed. The first two peaks (Onset 75 °C and 521.85 °C) can be assigned to the water removal and the dehydroxylation of the paste raw materials. Similar results were previously reported by Hajjaji et al. [45]. The major weight loss showed by the third peak (Onset 675 °C) may be attributed to the $CaCO_3$ decomposition and CO_2 formation. Similar results were found by Okada et al. [46] and Nandi et al. [47] who described the same thermal analysis for pastes with analogous constituents.

3.2. Tubular support manufacture

3.2.1. Casting

Extrusion has been used as the forming process of tubular support. For that, an extruder constructed by a local metallurgy company was used. The extruder was built in stainless steel with the specific requirements for obtaining tubular and monolithic ceramic supports. It essentially consists of a dope feed chamber, extruder screw shafts, mixing chamber, vacuum chamber, and the matrix with annular design. The inner and outer diameters of the annular matrix were 0.0095 m and 0.011 m, respectively.

The experimental protocol of supports casting was as follows: after ageing procedure, the green dopes were casted in gypsum plates until 20–30% dope humidity was reached. The drying mechanism of paste is mainly due to the capillary forces of the fine texture of the plaster pores. This paste has the appropriate fluidity or rheological properties to be extruded under pressure. The paste is passed through the nozzle with a screws speed of 5 rpm, paste scroll speed of 50 cm/min, in 65 cmHg of pressure. The green support was cut with a length 0.6 m, and then it was set into a gypsum cylindrical mould to avoid the twisting and bending effects during the drying process.

3.2.2. Drying and sintering theoretical fundaments

The drying and sintering of the green paste leads to ceramic structure consolidation. The heating schedule (temperature, heat-up rate and duration) was set according to the results of previous thermal studies [43]. A programmed temperature treatment allows the control of textural progress as well as the mechanical strength of the sintered samples. During this heat treatment, in a first stage (moderate temperatures) the paste loses humidity, whereas at higher temperatures the raw materials of the ceramic paste undergo structural changes and solid state reactions. Components of raw materials that have larger polymorphic and chemical changes are: silica, alumina and calcium carbonate. Silica has three polymorphic forms, quartz, tridymite and cristobalite, and each one has a structure of low (α) and high (β) temperature. The transformation from a structure into another is reversible and well defined. These high-low temperature transformations are just a change in bond angles and a slight adjustment of interatomic distances. The volume change produced by this rapid conversion is very important in the heat treatment, in particular the change of quartz at 573 °C from α to β structures corresponds to 2% of cubic expansion or contraction. The transformation rate may cause breakage or cracking of the moulded dry supports. The γ-alumina undergoes a series of transformations when subjected to heat treatments, appearing δ–θ phases with the increase of temperature and time. Because of the broad XRD peaks, it is difficult to make a distinction between γ and δ alumina. The θ-alumina transformation occurs at 900 °C, while the conversion to α-alumina more stable phase occurs at $T = 1150–1200$ °C, and this transformation is not reversible after cooling.

Changes that alter the chemical composition of the individual phases during sintering include chemical reactions in the solid state. An important feature of these reactions is that they are irreversible and the constituents remaining unchanged during the cooling process. Considering raw materials involved in the paste formulation, an important $CaCO_3$ decomposition reaction occurs in air to give CaO (s) and CO_2 (g) (T=825 °C). Another decomposition reaction that take place during the sintering process involves the kaolinite ($Al_2O_3 \cdot 2SiO_2 \cdot 2H_2O$), which at the temperature of 600 °C loses water to form mullite ($Al_2O_3 \cdot 2SiO_2$) and silica at 1000 °C [48]. Magnesium silicate present in the paste, decomposes at T= 800–840 °C forming ensteatite ($MgSiO_3$) and silica. The temperature range reported in some of the reactions was due to differences in particle size and the presence of impurities in the raw materials.

3.2.3. Drying and sintering experimental protocol

i) Drying: the green ceramic tubes were first slowly dried at environmental temperature (25 °C) during 24 h. Then, the drying process at higher temperature was conducted in an oven. The oven temperature was increased sequentially, 10 °C every 30 min from 50 °C to 110 °C.

ii) Sintering: the sintering process was made in the Nabertherm-Ceramotherm® N200 furnace (Germany), with automatic temperature controller. In order to avoid the appearance of cracks during both the α–β transition of quartz (573 °C) and the $CaCO_3$ calcinations (537 °C), two temperature ramps were used during the heating. In the first ramp the substrate was heated-up to 600 °C with a heating speed of 5 °C/min; while the second ramp the heat-up was carried out at 10 °C/min until reach the sintering temperature (T_s=1200 °C; 1300 °C; 1400 °C). The final temperature was kept constant for 30 min. After that, the consolidated support was allowed to cool until the environmental temperature was reached.

For strength resistance tests, parallelepipeds of 0.2 m length and square section of 0.015 m^2 were moulded and then sintered at different T_s.

3.3. Support characteristics

3.3.1. X-ray diffraction analysis

The three supports illustrated similar XRD patterns, showing coincidence in both appearance and intensity ratio of the diffraction peaks. XRD data for the S1 pattern sintered at 1200 °C are shown in Fig. 2(a). X-ray diffraction results clearly indicated that the most important crystalline phases recorded for all materials were those obtained at high temperatures. The main diffraction peaks were assigned to tridimite, crystobalite, γ-alumina, ensteatite by comparing with JCPDS data base file. These results are in agreement with the drying and sintering theoretical remarks previously reported in Section 3.2.

3.3.2. SEM micrograph

Fig. 3 shows SEM cross-section images of S1 support sintered at different temperatures. These cross-section images show a symmetric morphology, with big granules of approximately 100 μm (alumina, quartz and feldspar) and smaller particles (clay and bentonite) bounded each other, forming the primary vitrified skeletal structure of the alumina–silica with holes or pores. From these micrographs it is illustrated that the number of macro-voids decreases when the temperature increases, indicating the structures are related to sintering temperature. The three microphotographs have similar appearances; however Fig. 1(b) has less defined particle edges and Fig. 1(c) presents a higher degree of densification. Similar structural changes due to temperature of samples S2 and S3 were observed. At 1200 °C, the particles closely contacted each other and sintering in some extension at the edge of the grains forming interconnected network of pores. As temperature increases above 1200 °C the clay present in the paste begins to melt, binding the particles and reducing the porosity of the substrate. Furthermore, a significant densification and fewer amounts of macro-voids are observed when the sintering temperature reached 1400 °C. At this temperature, the silica begins to melt and flow around the remaining particles, resulting in a more compact and amorphous structure. Lee et al. [49], in their analysis of sintering temperature effect on ceramic prepared from clays, obtained analogous results.

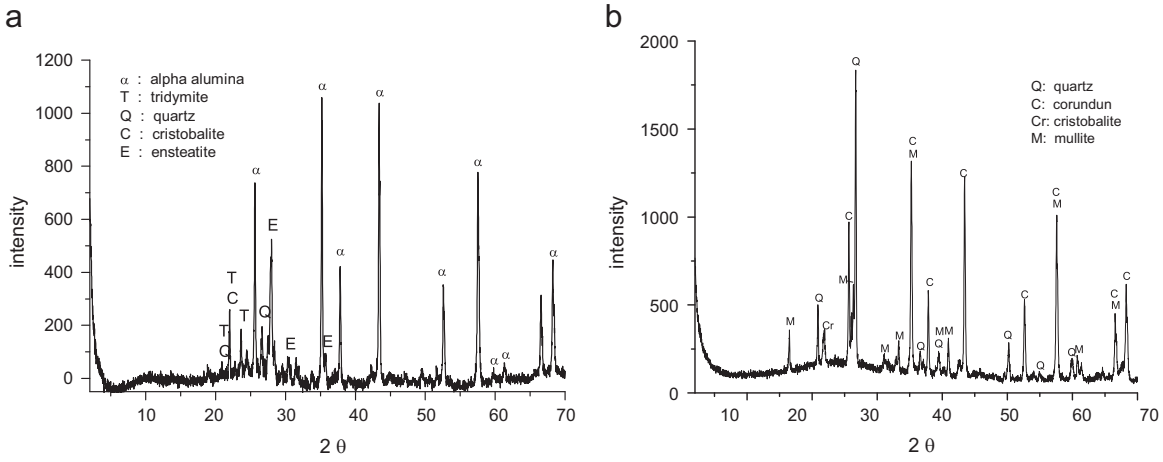

Fig. 2. X-ray diffractogram of: (a) S1 support and (b) A3 active layer.

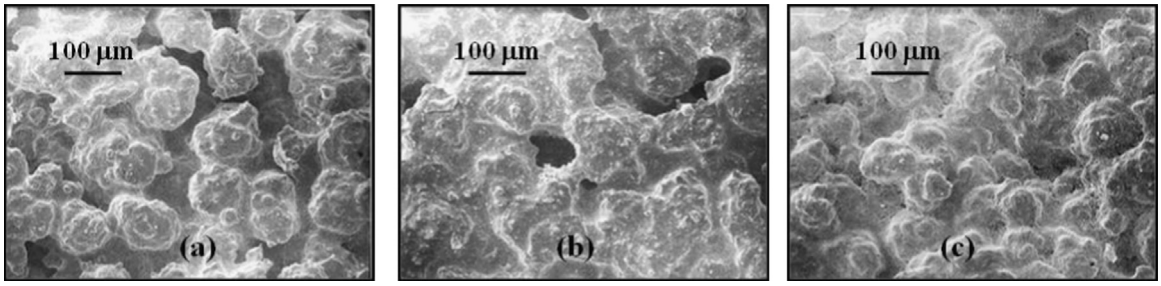

Fig. 3. SEM micrographs (750 ×) of S1 support: (a) T_s = 1200 °C; (b) T_s = 1300 °C; (c) T_s = 1400 °C.

Table 2
Structural and mechanical parameters of supports at different sintering temperatures.

Parameters	T_s = 1200 °C			T_s = 1300 °C			T_s = 1400 °C		
	S1	S2	S3	S1	S2	S3	S1	S2	S3
MIP Parameters									
Total pore area, A_p (m^2/g)	20.0	14.6	13.3	18.6	10.1	6.51	3.53	1.90	1.50
Mean pore radius (vol), r_v (μm)	15.7	22.6	20.6	21.6	25.9	26.7	15.6	24.2	21.1
Bulk density, ρ_b (g/ml)	1.62	1.56	1.63	1.70	1.72	1.75	2.58	2.40	2.62
Skeletal density, ρ_s (g/ml)	3.35	3.19	3.10	3.20	3.02	3.10	3.00	2.73	2.99
Porosity, ε (%)	51.8	51.2	47.3	48.7	43.0	39.6	13.8	12.2	11.8
MR parameter									
Fracture strength, σ (MPa)	16.7	17.5	19.1	17.2	18.6	26.4	20.2	24.8	34.2
WF parameters									
Support thickness, $l \times 10^3$ (m)	1.00	1.50	1.52	0.98	1.45	1.40	0.98	1.30	1.35
L_h (L m/h m^2 kPa)	2.76	5.04	0.68	1.64	3.55	0.46	0.71	2.31	0.27
Hydraulic pore size, r_h (μm)	3.86	5.25	2.01	3.07	3.27	1.80	3.80	7.28	2.53

3.3.3. Mercury intrusion porosimetry

The MIP results for the prepared supports are summarised in Table 2. Interesting support porosity (40–52%) and average pore size between 15 and 27 μm are shown. Similar porosities and pore size were reported in literature [50–52] for other type of ceramic based inorganic membrane. As expected, the pore size was influenced by the raw material composition and the mean particle size. S2 and S3 substrates have identical raw material compositions; nevertheless the S3 average particle size is lower than S2 (Table 1), which leads to S3 structure with smaller pore sizes. The S1 mean pore size was higher than S2, being inconsistent with the mean particle size (d_p(S1) > d_p(S2)). This inconsistency can be explained considering that S2 contains a greater amount of calcium carbonate than S1. The results showed that increasing the sintering temperature decreases the pore surface area and the porosity, being this reduction very significant at 1400 °C. Dong et al. [53] and Zhang et al. [54] obtained similar results when the effect of temperature on their porous substrates prepared from cordierite was analysed. The substrates sintered at 1200 °C (Fig. 4(a)) showed dual distribution of large pore sizes (in the macroporous range), approximately between 100 and 20 μm and 0.2–0.02 μm for S1 and S2 supports. Closer dual distributions were obtained for S3 support (≈ 20 to 6 μm and 2 to 0.5 μm), which can be attributed to the fact that the green paste was made from smaller particle sizes and without pore former ($CaCO_3$).

Fig. 4(b) shows the pore size distribution of S2 support at different sintering temperatures. This figure illustrates that when the temperature rises from 1200 to 1300 °C the distribution curve of smaller pores (< 0.2 μm) decreases, increasing consequently the average pore size. The distribution curve of smaller pore size practically disappears and the distribution curve of larger pore sizes (30–80 μm) decreases when sintering temperature was 1400 °C. In this case, the particles begin to melt, collapsing the smaller pores and reducing the volume and size of remaining pores. Similar behaviour of the temperature effect on pore size distribution for S2 and S3 was observed. These outcomes are consistent with the SEM observations.

3.3.4. Fracture strength

Fracture strength results from the sintered pattern bars prepared at different sintering temperatures are given in Table 2. The data showed an adequate increase of the fracture strength with the sintering temperature according to the substrate densification and the porosity decrease. Fig. 5 displays the porosity, mean pore size (from MIP) and fracture strength of S2 ceramic support as a function of sintering temperature. From 1200 to 1300 °C the fracture strength slightly increases, while the porosity and the bulk density decrease. Increasing sintering temperature from 1300 to 1400 °C, the substrates exhibited a significant increment in the bulk density and the fracture strength with a sharply decay in porosity, which are characteristics of relatively high densification.

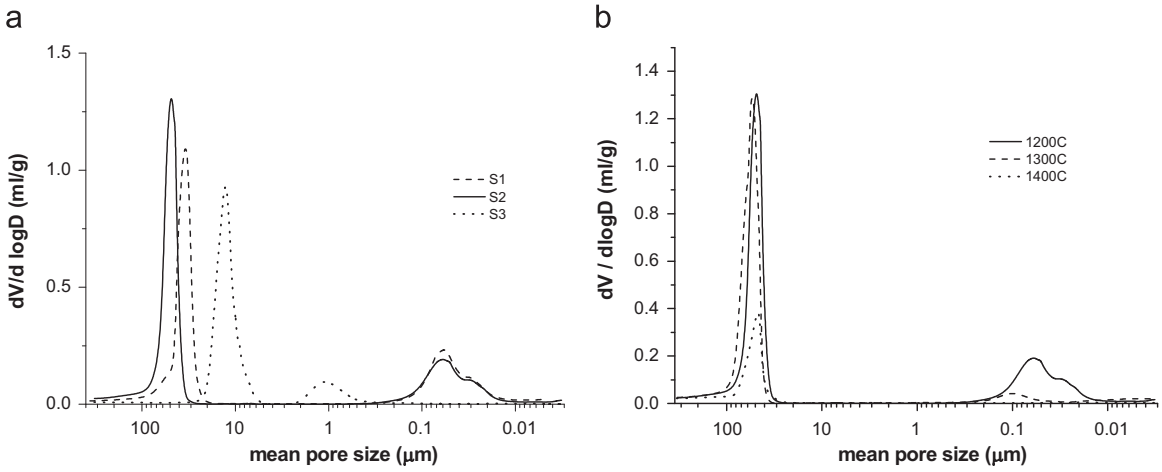

Fig. 4. Pore size distribution of: (a) S1, S2 and S3 supports (T_s = 1200 °C) and (b) S2 support at different temperatures.

3.3.5. Hydraulic permeability

Pure water filtration assays using the consolidated supports were performed. In contrast to the mercury intrusion tests, the water permeation through the ceramic supports provides information about actual pores, i.e. those pores interconnected from one face of the membrane to the opposite face [55]. Water permeation tests involved the measurement of filtering volume as a function of time at different transmembrane pressure (Δp = 0.7–30 kPa). Support patterns used in the water flow tests had the following geometrical dimensions: length $L \approx 0.2$ m, wall thickness (l) between 0.001 and 0.0015 m, and effective transfer area $A \approx 6.2 \times 10^{-4}$ m^2. Results showed a linear dependence of the water permeate flow with the pressure. The hydraulic permeability (L_h) was obtained from the slopes of J vs. Δp according to Eq. (2) and the r_h values evaluated from Eq. (3) ($\mu_w^{25\ °C} \approx 2.8 \times 10^{-7}$ Pa h). In the calculation of hydraulic radii the porosity obtained from MIP tests (Table 2) were used. The L_h and r_h data are shown in Table 2. In agreement with the conclusions obtained from the SEM micrographs and MIP studies, the hydraulic permeability and hydraulic pore radii decreased as the sintering temperature increased. It can be noted that the hydraulic radius was around one order of magnitude lower than the mean pore radius obtained from MIP measurements. This can be explained considering that the flow of water is controlled mainly by the interconnected pores of smaller sizes; whereas in the MIP technique takes into account not only actual pores but also other non-interconnected voids of the macro-porous matrix.

4. Active layer preparation and characterisation

4.1. Paste preparation

One of the main factors to control the porosity and pore size of the active layer is the particle size. To decrease the probability of cracking or fissures during the sintering process of the composite membrane, in the preparation of the active layer the same raw materials of the support were used. In the manufacture of the initial paste, the raw materials listed in Table 1 were added into distilled water (50% (w/w)) at 200 rpm of stirring rate

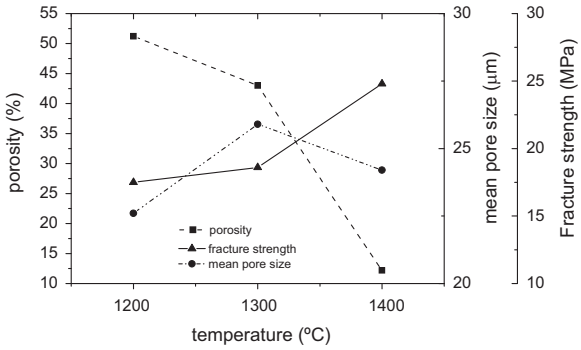

Fig. 5. Total porosity, mean pore size and fracture strength modulus of S2 support at different sintering temperatures.

during 2 h. From this paste four slurries with different particle sizes, identified as P1, P3, P5 and P7, were prepared. For that, the initial paste with an average particle diameter of 52.31 μm was crushed at different times of milling (t_m = 2, 3, 10, and 48 h) using a Retsch-PM4000 mill (Retsch GmbH, Germany). Particle size distributions determined by X-rays (Micromeritics SediGraph) showed that increasing the ball-milling time, the distribution curves of particles size were progressively narrowing.

The average particle diameters (d_p) obtained at different milling time are included in Table 3. The average particle diameter decreased considerably during the first 3 h of ball-milling process. Less pronounced decay of particle diameter at 10 and 48 h was observed. There was not a substantial change in the particles size distributions when the milling time was higher than 48 h.

The slurry fluidity mainly depends on the repulsion between the particles, among others factors. To improve rheological properties of the milled suspensions, such as deflocculation and plasticity, further sodium silicate ($\approx 0.02\%$ w/w) was added. Sodium silicate is a protective colloid that has the ability to reduce the particles tendency to flocculate. This compound is hydrolysed to silicic acid and free alkali, which act as a colloidal agent improving the dispersion properties of the inorganic precursors thereby addressing the homogeneity in the structure of the final substrate. The pastes were kept under stirring (200 rpm) during 2 days to ensure complete diffusion of the

Table 3
Characteristic parameters of pastes and active layers (T_s = 1200 °C).

Paste	t_m (h)	d_p (μm)	η (mPa s)	Active layer	MIP			Water flow		
					A_p (m^2/g)	ε (%)	r_v (μm)	$L_h \times 10^5$ (L m/h m^2 Pa)	$l \times 10^3$ (m)	r_h (μm)
P7	2	10.23	2900	A7	21.53	62.91	1.31	16.0	2.17	0.75
P5	3	6.48	2630	A5	24.72	63.44	0.77	8.02	1.94	0.51
P3	10	4.14	2320	A3	35.76	62.99	0.51	2.51	1.59	0.30
P1	48	2.40	2100	A1	51.84	63.52	0.22	0.55	1.05	0.14

components (paste ageing). To confer adequate casting properties, the suspensions were adjusted to a density of 1.5–1.6 g/cm^3. The density was determined with a digital density/specific gravimeter (Anton Paar, DMA 35, USA) and the viscosity was measured with a digital programmable viscometer (Brookfield-DVIII, USA). All the pastes showed tixotropic-pseudoplastic features, with viscosities ranging from 14,000 to 2000 cP at spindle rotation speed varying between 5 and 50 rpm, respectively. The apparent viscosity values (η) at 20 min of operation and constant spindle rotation speed of 50 rpm are listed in Table 3. These rheological properties allowed the pastes to be moulded by the flooding technique.

4.2. Active layer preparation

4.2.1. Paste casting, drying and sintering

Ceramic active layers were moulded by the casting method. Tubular 0.3 m length and 0.012 m of diameter mould configuration was used. Plaster moulds, once flooded with the green dope, absorb water and leads to a surface flocculation of the paste particles due to calcium sulphate. The crude ceramic elements were slowly dried at environmental temperature during 12 h and then they were put in a mechanical convection oven which temperature increased sequentially at a speed of 10 °C every 30 min from 50 °C to 110 °C. Neither cracks nor fissures were detected. Then, the dry tubes were sintered in the Nabertherm-Ceramotherm furnace. Two temperature ramps were used during the sintering process as it has been described in the experimental protocol for supports (Section 3.2). It has been shown [56] that the optimum sintering temperature of the active layer is between 1200 and 1300 °C. Lower temperatures give low consolidated structures for the ceramic material; while higher temperatures produce a collapse in the porous structure. According with the sintered support results and the conclusions arrived in previous works [43,56] the sintering temperature of 1200 °C for the active layer was selected. The consolidated active layers were identified as A1, A3, A5 and A7, corresponding to pastes P1, P3, P5 and P7, respectively.

4.2.2. Chemical and structural characteristics

4.2.2.1. X-ray diffraction. In order to determine the crystalline compounds present in the sintered active layers X-ray diffraction tests were performed. Fig. 2(b) shows the diffractogram obtained for A3 active layer. The diffractogram shows diffraction lines (peaks) corresponding to cristobalite (silica phase at high temperature), mullite (a stable phase at high temperatures in the SiO_2–Al_2O_3 diagram at atmospheric pressure), corundum (alumina phase at high temperature) and quartz, according to JCPDS data base file. As the active layer pastes have the same formulation, their diffractograms were coincident.

4.2.2.2. Mercury intrusion porosimetry. The average pore diameter and pore size distribution in porous active layers were determined from mercury intrusion porosimetry. These tests showed a bimodal pore size distribution curves for the active layers sintered at 1200 °C. The main structural parameters, pore area (A_p), porosity (ε) and mean pore radius (r_v) are summarised in Table 3. There is not a substantial change on the porosity values ($\varepsilon \approx 63\%$), and the mean pore size follow the expected general trends, increases as average particle size of the pastes increases. These results are in concordance with the remarks given by Kim et al. [57] in which the porosity principally depends on the sintering temperature, while the pore size is mainly dependent on the size of the starting powder used for the membrane manufacture.

4.2.2.3. Hydraulic permeability. As it was previously pointed out (Section 3.3.4), water fluxes at different membrane pressure provide the hydraulic permeability and a suitable approximation about of the "mean effective pore radius". In the experimental procedure, the tubular membranes of active layers, length $l \approx 0.3$ m, internal diameter ID ≈ 0.01 m, were placed in the permeation module. From the slopes of water flow vs. trans-membrane pressure graphs (Δp between 10 and 100 kPa), the hydraulic permeability and the hydraulic pore radius were obtained from Eqs. (2) and (4). In the hydraulic radii calculation, the porosity (ε) obtained from MIP tests (Table 2) were used. The L_h and r_h values for the different active layers are summarised in Table 3.

Pore radii obtained by the MIP were 1.5–1.7 times higher than those obtained from hydraulic permeability technique. As it was remarked in Section 3.3.4, the mercury porosimetry gives bigger pores because it detects not only actual pores but also other non-interconnected voids of the porous matrix. The most appropriate radius values are those obtained by hydraulic permeability because they are directly related with the liquid flow for filtration processes. In this case, the hydraulic pore radii or the A1, A3, A5 and A7 active layers were 0.15, 0.30, 0.51 and 0.75 μm, respectively, being these pore radii suitable for the microfiltration process.

5. Composite membrane manufacture and characteristics

5.1. Manufacture

One of the most applied methods to make supported active layers is by dip-coating technique. In this work, the coating technique consisted of flooding the active layer inside of the tubular support and, after a suitable residence time, the remaining barbotine was discharged. The selection of the support to be used as substrate in the preparation of the microfiltration CM was made on the basis of their structural and mechanical characteristics. If the characteristics of the S1, S2 and S3 supports at T_s = 1200 °C (Table 2) are analysed, it can be seen that the values of porosity (ε) and strength modulus (σ) are analogous; however, the S2 support has the higher pore size and hydraulic permeability, so it was selected to prepared composite membrane.

According to the diagram shown in Fig. 1, the manufacture protocol of the composite membrane consisted of:

i – S2 support was prepared following the protocol given in Section 3.2. The support was burned at a final temperature of $T=1000$ °C (bisque or partially fired). The obtained support possessed a cake-like structure with a high porosity ($\varepsilon \approx 70\%$) and low mechanical strength ($\sigma \approx 10$ MPa); however, it was strong enough to be handled during the slip-casting process with the barbotine of the active layer. These properties of the support enable to avoid the formation of fissures or cracks in the active layer during the sintering procedure of the composite membrane.

ii – P1, P3, P5 and P7 pastes were used as coating suspensions. Pastes preparation follows the procedure described in Section 4.1. Prior to the casting process, the pastes were adjusted to a specific gravity of 1.2 g/cm^3; minimum density value at which the paste begins to flocculate and the appropriate paste fluidity is reached. These were the best rheological characteristics of barbotine to be used in the slip-casting process.

iii – The different CM were prepared by slip-casting of the aged and adjusted pastes (part ii) onto the internal surface of bisque support. The barbotines were flooded on the inner part of the tubular support. The same residence dipping time for all the pastes ($t=13\pm2$ s) was used. This period of time was the minimum required to fill up and discharge the suspensions inside the tubular supports (outer diameter 0.011 m, wall thickness 0.0015 m and length 0.3 m). After drying at room temperature and in an oven at 120 °C the CM were sintered following the temperature rising programme described in the sintering experimental procedure (Section 3.2); that is an initial temperature increase to 500 °C with a heating rate of 4 °C/min, a second ramp with a more pronounced rate (6 °C/min) to a $T=800$ °C, then a rise in temperature at a heating rate of 10 °C/min to the final sintering temperature of $T_s=1200$ °C, which was maintained for 30 min. To determine the effect of sintering temperature on the composite membrane structure, final T_s of 1300 °C and 1400 °C were also investigated. The four CM obtained from the S2 support and pastes of A1, A3, A5, A7 active layers were designated as S2A1, S2A3, S2A5 and S2A7, respectively.

5.2. Characteristics of composite membranes

5.2.1. SEM analysis

Cross section morphology of consolidated composite membrane and the presence of possible defects were observed by using a scanning electron microscope. Substrates were fractured and sputter-coated with gold under low vacuum. Fig. 6 shows the microphotographs of the cross section of the S2A3 composite membrane sintered at different temperatures. The photomicrograph of the composite membrane sintered at 1200 °C (Fig. 6(a)) shows two well-defined regions, one corresponding to the support formed by macro-pores and macro-particles, and the other to the thin active layer region formed by pores and particles of smaller sizes. Between the active layer and the support a denser interface can be appreciated, in which part of the macro-pores of the support have been flooded by the material of the active layer. This can be explained considering that during the dip-coating process, the water and the smaller particles from the paste are introduced into the pores of the support by capillary force and a thin layer is formed by deposition of particles at the support-suspension boundary. Smaller particles deposited in the pores of the support shrunk significantly during the sintering process, leading to a denser structure at the support-active layer interface. It can be noted that when the sintering temperature is raised to 1300 °C there was a further densification of the active layer (Fig. 6(b)), while at 1400 °C the collapse of the pores and the vitrification of the whole structure was remarkable (Fig. 6(c)). Similar structures for S2A1, S2A5, S2A7 composite membranes, prepared at different sintered temperatures, were obtained. The S2 support thickness was $l_{S2}=1.5\pm0.2\times10^{-3}$ m and the average active layer thickness (l_{Ai}) of the CM ($T_s=1200$ °C) determined from SEM observations are included in Table 4.

5.2.2. Hydraulic permeability

Since the effective thickness of the composite membrane is not known, the hydraulic permeability expressed as L'_h was evaluated from the slope representing the permeated water flow vs. the transmembrane pressure according to Eq. (3). Table 4 shows the values of L'_h obtained for different CM. The relatively high hydraulic permeability showed by the composite membranes may be mainly due to their structural properties, high total porosity and support pore size, and adequate active layer pore size.

As stated, the composite membrane consists of two ceramic substrates in series, the S2 support and the Ai active layer ($i=1, 3, 5, 7$). Assuming that the S2–Ai interface is well defined (the substrates kept their intrinsic properties) it can be considered that the total resistance of the composite membrane (R_T) is given by the support resistance (R_{S2}) plus the resistance of the active layer (R_{Ai}). From Eq. (2), the total and individual

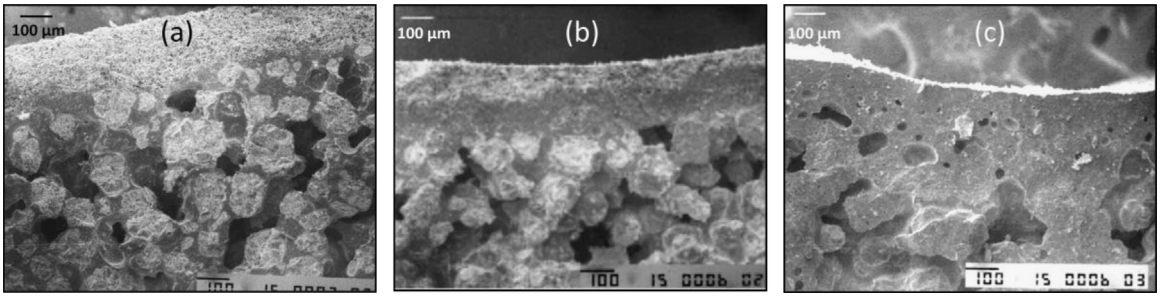

Fig. 6. SEM micrographs of S2A3 composite membrane, (a) 1200 °C, (b) 1300 °C, (c) 1400 °C.

Table 4
Physical and structural parameters of composite membranes.

CM	$l_{Ai} \times 10^6$ (m)	L'_h (L/h m^2 kPa)	$R_{S2} \times 10^{-9}$ (m^{-1})	$R_{Ai} \times 10^{-9}$ (m^{-1})	$R_T \times 10^{-9}$ (m^{-1})	r_h (CM) $\times 10^6$ (m)
S2A1	205 ± 15	9.90 ± 0.6	1.07	133.0	133.2	0.085
S2A3	223 ± 19	26.3 ± 1.3	1.07	31.46	32.53	0.144
S2A5	268 ± 18	46.6 ± 2.8	1.07	13.08	14.15	0.211
S2A7	305 ± 25	273.5 ± 14	1.07	6.885	7.955	0.545

Table 5
Hydraulic permeability of different composite membrane.

Composite membranes		r_h (CM) (μm)	$L'_h \times 10^3$ (L/h m^2 Pa)
Present Work	S2A1	0.085	9.90
	S2A3	0.144	26.3
	S2A5	0.211	46.6
	S2A7	0.545	273.5
Jiuwu High-Tech Co. Ltd. [58]		0.20	5.23
		0.50	8.91
Carbosep [59]		0.45	1.77
CeRAM™ TAMI Industries [60]		0.1	3.42
Masmoudi et al. [61]		0.50	5.85
Khemakhem et al. [4]		0.20	8.70
Jedidi et al. [62]		0.25	4.75

substrates resistances are given by:

$$R_{T(S2Ai)} = R_{S2} + R_{Ai} = \left(\frac{l}{\mu L_h}\right)_{S2Ai} = \left(\frac{l}{\mu L_h}\right)_{S2} + \left(\frac{l}{\mu L_h}\right)_{Ai} \quad (5)$$

The R_T, R_{S2}, and R_{Ai} data obtained from l_{Ai} and L_h (Table 3) values are included in Table 4. It can be noted that the resistance values of the active layer were very close to those of total resistances (99–87%). From this, it is valid to consider the total composite membrane resistance is mainly due to the active layer resistance. Therefore, the hydraulic radius of each composite membrane can be approximately estimated from Eq.(4), using the l_{Ai} and L'_h experimental data. The composite membrane r_h data are informed in Table 4. CM r_h values were 1.4–2.4 times lower than those of the active layer (Table 3). According to comments made in the analysis of SEM microphotographs, this can be attributed to densification occurred in the support-active layer interface, leading to a decrease in pore size. L'_h data of the composite ceramic membranes prepared in this study are compared with values reported by other researchers and commercial membranes (Table 5). These results show the high performance of the CM prepared in this work.

5.3. CM experimental tests

The effectiveness of the ceramic CM was tested through microfiltration tests of different substances from food industry, such as slaughterhouse wastewater and goat milk.

5.3.1. Slaughterhouse wastewater treatment

The effluent treatment plant from slaughterhouses needs to be designed to reduce the parameter levels of contaminants such as chemical oxygen demand (COD), oil and fat, suspended solids, and pathogens, among others. A pre-treatment is usually performed by fences and traps to retain solids and fats. Then, a primary treatment that involves the removal of a significant amount of suspended solids contained in the wastewater by physical and chemical processes (addition of chemical flocculants) is applied. Finally, the effluent is subjected to a secondary biological treatment.

Pre-treated slaughterhouse effluent was used as feed solution in the microfiltration test. S2A1 composite ceramic membrane was utilised in wastewater treatment at bench scale (membrane transfer area 0.037 m^2). The operating pressure (100 kPa), temperature (T=25 °C), and feed flow velocity (v=3.18 m/s) were kept constant. A continuous decline in permeate flux (initial flux $J_0 \approx 430$ L/h m^2) was observed within the first hour. Afterwards, the permeate flux started to be stabilized and remain constant reaching the pseudo steady state ($J_\infty \approx 110$ L/h m^2). Feed and permeate wastewater physicochemical and bacteriological characteristics are included in Table 6. The bacterial removal (CAV) and COD rejection were 99.4% and 91%, respectively, whereas the total hydrocarbons retention was 33%. Similar results were obtained in previous work [43] using unsupported ceramic active layer.

5.3.2. Microfiltration of goat milk

Microfiltration of milk has the advantage of reducing the amount of bacteria and spores without affecting the taste of the milk and extending the lifetime of the milk regarding to other pasteurisation processes such as UHT process. In order to determine the performance of composite ceramic membranes in the microfiltration of milk, bench scale tests with goat milk provided by a local dairy farm were performed. For that, S2A7 and S2A1 composite membranes were used. The operating conditions were: feed rate 4 L/min, transmembrane pressure 72 kPa, and temperature T=30 °C. Results showed a significant drop in permeate fluxes for both membranes during the first two hours of operation, then becoming nearly constant reaching quasi-stationary conditions.

Table 6 shows the physicochemical parameters of milk in the feed and permeate streams. Results showed that soluble compounds were not rejected by the membranes, whereas fats were partially retained. It is noteworthy the high degree of pasteurisation of goat milk obtained in the permeate solution with bacteria rejections of 67% (S2A7) and 82% (S2A1), maintaining almost constant the other physicochemical properties of the original milk.

6. Conclusions

In this work, a comprehensive study on the fabrication and characterisation of composite ceramic membranes from

Table 6
Physicochemical- bacteriological parameters and steady state permeate flows.

Parameters	Slaughterhouse wastewater		Goat milk		
	Feed	Permeate S2A1	Feed	Permeate S2A7	Permeate S2A1
pH	7.95	7.80	7.44	7.42	7.42
Turbidity (g/L $CaSO_4$)	0.92	0.025	–	–	–
Density (g/cc) (20 °C)	–	–	1.03	1.03	1.03
COD (ppm de O_2)	480	45.0	–	–	–
Total acidity	–	–	15	14.5	14.1
Total N (ppm)	115	63.0	–	–	–
Fat materials (g/100 ml)	–	–	4.23	3.61	3.36
Total C (ppm)	183	101	–	–	–
Proteins (%, w/w)	–	–	4.13	3.65	3.71
CAV (count/ml) $\times 10^{-6}$	42.0	0.24	0.13	0.043	0.023
Initial and steady state permeate flow (L/h m^2)	430	110	80–75	13.0	4.50

aluminosilicates was performed. The proposed methodology allows obtaining supports, active layers and composite membranes suitable for being used in microfiltration processes. The membrane support was prepared by the extrusion procedure using a ceramic paste made with raw materials such as ball clay, bentonite, quartz, feldspar, alumina and the addition of additives. The mechanical and structural properties of the tubular supports sintered at $T_s = 1200$ °C were adequate with high strength modules (17–19 MPa) and porosities (> 50%), as well as suitable hydraulic pore sizes (2–5.5 μm).

Active layer pastes with different mean particle sizes were prepared using the same raw materials employed in the support paste and milling the paste during different periods of time. After rheological adjustment, the pastes were moulded by the casting method in plaster moulds with tubular configuration. The tubular unsupported active layers were dried and sintered at $T_s = 1200$ °C. The active layer substrates showed remarkable structural properties, high porosity (≈ 63%) and hydraulic pore size ranging from 0.14 to 0.75 μm. Four CM were prepared by flooding the inside of the S2 tubular support with different active layer pastes. After drying and sintering procedure ($T_s = 1200$ °C) the tubular composite membranes showed the following structural characteristics: overall porosity $\varepsilon > 51\%$, support thickness, $l_{S2} = 1.5 \pm 0.2 \times 10^{-3}$ m; active layer thickness between 205 and 305 μm; effective hydraulic pore sizes of 0.085, 0.14, 0.21, and 0.55 μm. Water flux tests pointed out the high hydraulic permeability of CM ranging from 10 to 274 L/h m^2 kPa.

Efficiency of CM for slaughterhouse wastewater treatment and goat milk sterilisation were studied. The noticeable characteristics of permeate solutions, high rejection of insoluble residue and bacterial removal; suggest that S2A1, S2A3, S2A5, and S2A7 synthesised CM are suitable for a real application in microfiltration processes. Prepared ceramic membranes of microfiltration resulted good candidates for interesting separations in food industries.

Acknowledgements

The authors acknowledge the National Agency for Scientific Promotion (ANPCyT) PICT 2008-2184, University of San Luis Project PROICO 2-1712, and University of Rio Cuarto PICT 2011-2144 for their financial support.

References

[1] L. Xu, W. Li, S. Lu, Z. Wang, Q. Zhu, Y. Ling, Treating dyeing waste water by ceramic membrane in crossflow microfiltration, Desalination 149 (2002) 199–203.
[2] M. Ebrahimi, K. Shams Ashaghi, L. Engel, D. Willershausen, P. Mund, P. Bolduan, P. Czermak, Characterization and application of different ceramic membranes for the oil-field produced water treatment, Desalination 245 (2009) 533–540.
[3] S. Masmoudi, R. Ben Amar, A. Larbot, H. El Feki, A. Ben Salah, L. Cot, Elaboration of inorganic microfiltration membranes with hydroxyapatite applied to the treatment of wastewater from sea product industry, J. Membr. Sci. 247 (2005) 1–9.
[4] S. Khemakhem, R. Ben Amar, R. Ben Hassen, A. Larbot, M. Medhioub, A. Ben Salah, L. Cot, New ceramic membranes for tangential waste-water filtration, Desalination 167 (2004) 19–22.
[5] S. Mahesh Kumar, G.M. Madhu, Sukumar Roy, Fouling behaviour, regeneration options and on-line control of biomass-based power plant effluents using microporous ceramic membranes, Sep. Purif. Technol. 57 (2007) 25–36.
[6] B.K. Nandi, B. Das, R. Uppaluri, M.K. Purkait, Microfiltration of mosambi juice using low cost ceramic membrane, J. Food Eng. 95 (2009) 597–605.
[7] F. Vaillant, A. Millan, M. Dornier, M. Decloux, M. Reynes, Strategy for economical optimisation of the clarification of pulpy fruit juices using cross flow microfilltration, J. Food Eng. 48 (2001) 83–90.
[8] B.J. Wang, T.C. Wei, Z.R. Yu, Effect of operating temperature on component distribution of West Indian cherry juice in a microfiltration system, LWT 38 (2005) 683–689.
[9] H. Lucena Lira, M.C. Delgado da Silva, M.R. dos Santos Vasconcelos, H. Lucena Lira, A.M. Queijeiro Lopez, Microfiltração do soro de leite de búfala utilizando membranas cerâmicas como alternativa ao processo de pasteurização, Ciênc. Tecnol. Aliment 29 (2009) 33–37.
[10] J. Zulewska, M. Newbold, D.M. Barbano, Efficiency of serum protein removal from skim milk with ceramic and polymeric membranes at 50 °C, J. Dairy Sci. 92 (2009) 1361–1377.
[11] V.S. Espina, M.Y. Jaffrin, M. Frappart, L.H. Ding, Separation of casein micelles from whey proteins by high shear microfiltration of skim milk using rotating ceramic membranes and organic membranes in a rotating disk module, J. Membr. Sci. 325 (2008) 872–879.
[12] L.V. Saboya, J.-L. Maubois, Current developments of microfiltration technology in the dairy industry, Lait 80 (2000) 541–553.
[13] Y. Pouliot, Membrane processes in dairy technology – from a simple idea to worldwide panacea, Int. Dairy J. 18 (2008) 735–740.
[14] R. Ohashi, E. Mochizuki, T. Suzuki, A. Mini-Scale Mass, Production and separation system for secretory heterologous proteins by perfusion culture

of recombinant pichia pastoris using a shaken ceramic membrane flask, J. Biosci. Bioeng. 87 (1999) 655–660.
[15] P.M. Kao, S.C. Huang, Y.C. Chang, Y.C. Liu, Development of continuous chitinase production process in a membrane bioreactor by *Paenibacillus sp*. CHE-N1, Process Biochem. 42 (2007) 606–611.
[16] A.J. Burggraaf, L. Cot, in: Fundamentals of Inorganic Membrane Science and Technology, Elsevier Science, Amsterdam, The Netherlands, 1996.
[17] K. Li, Ceramic Membranes for Separation and Reaction, John Wiley and Sons Ltd, West Sussex, England, 2007.
[18] M.C. Schillo, I.-S. Park, W.V. Chiu, H. Verweij, Rapid thermal processing of inorganic membranes, J. Membr. Sci. 362 (2010) 127–133.
[19] J. Zhu, Y. Fan, N. Xu, Preparation and characterization of alumina membranes on capillary supports: effect of film-coating on crack-free membrane preparation, Chin. J. Chem. Eng. 3 (2010) 377–383.
[20] W. Qin, C. Peng, M. Lv, J. Wu, Preparation and properties of high-purity porous alumina support at low sintering temperature, Ceram. Int. 40 (2014) 13741–13746.
[21] S. Yoo, S. Yeu, R.L. Sherman, E.E. Simanek, D.F. Shantz, D.M. Ford, Reverse-selective membranes formed by dendrimers on mesoporous ceramic supports, J. Membr. Sci. 334 (2009) 16–22.
[22] G. Li, H. Qi, Y. Fan, N. Xu, Toughening macroporous alumina membrane supports with YSZ powders, Ceram. Int. 35 (2009) 1641–1646.
[23] H. Bissett, J. Zah, H.M. Krieg, Manufacture and optimization of tubular ceramic membrane supports, Powder Technol. 181 (2008) 57–66.
[24] C. Liu, L. Wang, W. Ren, Z. Rong, X. Wang, J. Wang, Synthesis and characterization of a mesoporous silica (MCM-48) membrane on a large-pore α-Al_2O_3 ceramic tube, Microporous Mesoporous Mater. 106 (2007) 35–39.
[25] B. Ernst, S. Haag, M. Burgard, Permselectivity of a nickel/ceramic composite membrane at elevated temperatures: a new prospect in hydrogen separation?, J Membr. Sci. 288 (2007) 208–217.
[26] S. Haag, M. Burgard, B. Ernst, Pure nickel coating on a mesoporous alumina membrane: preparation by electroless plating and characterization, Surf. Coat. Technol. 201 (2006) 2166–2173.
[27] J. Carretero, J.M. Benito, A. Guerrero-Ruiz, I. Rodrıguez-Ramos, M.A. Rodrıguez, Infiltrated glassy carbon membranes in γ-Al_2O_3 supports, J. Membr. Sci. 281 (2006) 500–507.
[28] N.L. de Freitas, J.A.S. Goncalves, M.D.M. Innocentini, J.R. Coury, Development of a double-layered ceramic filter for aerosol filtration at high-temperatures: the filter collection efficiency, J. Hazard. Mater. B136 (2006) 747–756.
[29] D. Kim, A. Kellogg, E. Livaich, B.A. Wilhite, Towards an integrated ceramic micro-membrane network: electroless-plated palladium membranes in cordierite supports, J. Membr. Sci. 340 (2009) 109–116.
[30] Y. Dong, X. Feng, D. Dong, S. Wang, J. Yang, J. Gao, X. Liu, G. Meng, Elaboration and chemical corrosion resistance of tubular macro-porous cordierite ceramic membrane supports, J. Membr. Sci. 304 (2007) 65–75.
[31] L. Zhou, T. Wang, Q.T. Nguyen, J. Li, Y. Long, Z. Ping, Cordierite-supported ZSM-5 membrane: preparation and pervaporation properties in the dehydration of water–alcohol mixture, Sep. Purif. Technol. 44 (2005) 266–270.
[32] G. Chen, H. Qi, W. Xing, N. Xu, Direct preparation of macroporous mullite supports for membranes by in situ reaction sintering, J. Membr. Sci. 318 (2008) 38–44.
[33] M. Asghari, T. Mohammadi, A. Aziznia, M.R. Danayi, S.H. Moosavi, R.F. Alamdari, F. Agand, Preparation and characterization of a thin continuous faujasite membrane on tubular porous mullite support, Desalination 220 (2008) 65–71.
[34] S. Masmoudi, A. Larbot, H. El Feki, R. Ben Amar, Elaboration and characterisation of apatite based mineral supports for microfiltration and ultrafiltration membranes, Ceram. Int. 33 (2007) 337–344.
[35] N. Saffaj, M. Persin, S.A. Younsi, A. Albizane, M. Cretin, A. Larbot, Elaboration and characterization of microfiltration and ultrafiltration membranes deposited on raw support prepared from natural Moroccan clay: application to filtration of solution containing dyes and salts, Appl. Clay Sci. 31 (2006) 110–119.
[36] L. Palacio, Y. Bouzerdi, M. Ouammou, A. Albizane, J. Bennazha, A. Hernández, J.I. Calvo, Ceramic membranes from Moroccan natural clay and phosphate for industrial water treatment, Desalination 245 (2009) 501–507.
[37] S. Jana, M.K. Purkait, K. Mohanty, Preparation and characterization of low-cost ceramic microfiltration membranes for the removal of chromate from aqueous solutions, Appl. Clay Sci. 47 (2010) 317–324.
[38] A. Harabi, F. Zenikheri, B. Boudaira, F. Bouzerara, A. Guechi, L. Foughali, A new and economic approach to fabricate resistant porous membrane supports using kaolin and $CaCO_3$, J. Eur. Ceram. Soc. 34 (2014) 1329–1340.
[39] A. Harabi, A. Guechi, S. Condom, Production of supports and filtration membranes from algerian kaolin and limestone, Procedia Eng. 33 (2012) 220–224.
[40] P.K. Tewari, R.K. Singh, V.S. Batra, M. Balakrishnan, Membrane bioreactor (MBR) for wastewater treatment: filtration performance evaluation of low cost polymeric and ceramic membranes, Sep. Pur. Technol. 71 (2010) 200–204.
[41] Y. Dong, X. Liu, Q. Ma, G. Meng, Preparation of cordierite-based porous ceramic micro-filtration membranes using waste fly ash as the main raw materials, J. Membr. Sci. 285 (2006) 173–181.
[42] J. Cao, X. Dong, L. Li, Y. Dong, S. Hampshire, Recycling of waste fly ash for production of porous mullite ceramic membrane supports with increased porosity, J. Eur. Ceram. Soc. 34 (2014) 3181–3194.
[43] M.C. Almandoz, J. Marchese, P. Prádanos, L. Palacio, A. Hernández, Preparation and characterization of non-supported microfiltration membranes from aluminosilicates, J. Membr. Sci. 241 (2004) 95–103.
[44] J. Marchese, M. Amaral, J. Encabo, C. Almandoz, in: J. Gaballah, R., Hager, R. Solozabal (Eds.), Application of Ceramic Membranes to Slaughterhouse Wastewater Treatment, vol. III, The Minerals Metals & Materials Society, Warrendale, PA, U.S.A, 1999, pp. 2377–2385.
[45] M. Hajjaji, S. Kacim, A. Alami, A. El Bouadili, M. Mountassir, Chemical and mineralogical characterization of a clay taken from the Moroccan Meseta and a study of the interaction between its fine fraction and methylene blue, Appl. Clay Sci. 20 (2001) 1–12.
[46] K. Okada, N. Watanabe, K.V. Jha, Y. Kameshima, A. Yasumori, K.J.D. MacKenzie, Effects of grinding and firing conditions on $CaAl_2Si_2O_8$ phase formation by solid-state reaction of kaolinite with $CaCO_3$, Appl. Clay Sci. 23 (2003) 329–336.
[47] B.K. Nandi, R. Uppaluri, M.K. Purkait, Preparation and characterization of low cost ceramic membranes for micro-filtration applications, Appl. Clay Sci. 42 (2008) 102–110.
[48] A. Ghorbel, M. Fourati, J. Bouaziz, Microstructural evolution and phase transformation of different sintered Kaolins powder compacts, Mater. Chem. Phys. 112 (2008) 876–885.
[49] V.-G. Lee, T.-H. Yeh, Sintering effects on the development of mechanical properties of fired clay ceramics, Mater. Sci. Eng. A 485 (2008) 5–13.
[50] J.M. Benito, A. Conesa, F. Rubio, M.A. Rodrıguez, Preparation and characterization of tubular ceramic membranes for treatment of oil emulsions, J. Eur. Ceram. Soc. 25 (2005) 1895–1903.
[51] S.-H. Lee, K.-C. Chung, M.-C. Shin, J.-I. Dong, H.-S. Lee, K.H. Auh, Preparation of ceramic membrane and application to the crossflow microfiltration of soluble waste oil, Mater. Lett. 52 (2002) 266–271.
[52] S. Khemakhem, A. Larbot, R. Ben Amar, New ceramic microfiltration membranes from Tunisian natural materials: application for the cuttlefish effluents treatment, Ceram. Int. 35 (2009) 55–61.
[53] Y. Dong, B. Lin, S. Wang, K. Xie, D. Fang, X. Zhang, H. Ding, X. Liu, G. Meng, Cost-effective tubular cordierite micro-filtration membranes processed by co-sintering, J. Alloy. Compd. 477 (2009) L35–L40.
[54] X. Zhang, D. Fang, B. Lin, Y. Dong, G. Meng, X. Liu, Asymmetric porous cordierite hollow fiber membrane for microfiltration, J. Alloy. Compd. 487 (2009) 631–638.
[55] R.R. Bhave, Liquid filtration and separation with inorganic membranes, in: R.R. Bhave (Ed.), Inorganic Membranes: Synthesis, Characteristics, and Applications, Chapman & Hall, New York, London, 1991, pp. 129–154.
[56] M.C. Almandoz, Membranas cerámicas de microfiltración: Preparación, caracterización y aplicaciones (Doctoral thesis), Universidad Nacional de San Luis, San Luis, Argentina, 2009.

[57] K.-H. Kim, S.-J. Cho, K.-J. Yoon, J.-J. Kim, J. Ha, D. Chun, Centrifugal casting of alumina tube for membrane application, J. Membr. Sci. 199 (2002) 69–74.

[58] H. Zhang, Z. Zhong, X. Li, W. Xing, W. Jin, River water purification via a coagulation-porous ceramic membrane hybrid process, Chin. J. Chem. Eng. 22 (2014) 113–119.

[59] M.D. Afonso, A.M. Brites A1ves, M. Mohsen, Crossflow microfiltration of marble processing wastewaters, Desalination 149 (2002) 153–162.

[60] X. Zhang, L. Fan, F.A. Roddick, Understanding the fouling of a ceramic microfiltration membrane caused by algal organic matter released from *Microcystis aeruginosa*, J. Membr. Sci. 447 (2013) 362–368.

[61] S. Masmoudi, R. Ben Amar, A. Larbot, H. El Feki, A. Ben Salah, L. Cot, Elaboration of inorganic microfiltration membranes with hydroxyapatite applied to the treatment of wastewater from sea product industry, J. Membr. Sci. 247 (2005) 1–9.

[62] I. Jedidi, S. Saïdi, S. Khemakhem, A. Larbot, N. Elloumi-Ammar, A. Fourati, A. Charfi, R. Ben Amar, Elaboration and characterisation of fly ash based mineral supports for microfiltration and ultrafiltration membranes, Ceram. Int. 35 (2009) 2747–2753.